EVALUATING THE QUALITY OF SYNTHETIC IMAGES OF POROUS MEDIA: A MORPHOLOGICAL AND PHYSICS-BASED APPROACH

Kelly M. Guan* **& Anthony R. Kovscek**
Department of Energy Resources Engineering
Stanford University
Stanford, CA 94305, USA
{kmguan,kovscek}@stanford.edu

Timothy I. Anderson
Department of Electrical Engineering
Stanford University
Stanford, CA 94305, USA
timothy.anderson@stanford.edu

Patrice Creux
Universite de Pau et des Pays de l'Adour
E2S UPPA, CNRS, TOTAL, LFCR
Pau, France
patrice.creux@univ-pau.fr

ABSTRACT

One area of intense scientific interest for the study of sandstones, carbonates, and shale at the pore scale is the use of limited image and petrophysical data to generate multiple realizations of a rock's pore structure. We develop and evaluate a deep learning-based method to synthesize porous media volumes from 2D training images using a generative flow model trained on x-ray computed tomography images of rock texture and pore structure. These models are optimized on a log-likelihood objective and are shown to synthesize large and realistic 3D images. Realism is gauged by quantitative comparison of topological features using Minkowski functionals. We also evaluate the single-phase permeability and show that physics-based transport properties of the generated samples match measured trends.

1 INTRODUCTION

Porous medium properties, such as porosity and permeability, are often calculated from laboratory measurements or direct imaging of the rock microstructure (Walsh & Frangos, 1968; Ketcham & Carlson, 2001). Due to acquisition times and experimental costs, however, it is difficult to acquire multiple datasets to evaluate the variability of these properties, especially as sample permeability decreases. Researchers therefore often use computational methods to reconstruct porous media based on statistical properties (Okabe & Blunt, 2007). Recently, researchers have applied deep generative models, specifically GANs, to reconstruct porous systems from limited rock image datasets (Mosser et al., 2017; Feng et al., 2019). Advantages of using deep learning-based over stochastic methods are rapid generation of the images, especially in 3D, and removing the necessity of incorporating physical parameters that must be predetermined *a priori* from the rock dataset.

Here we consider flow-based models due to the model's scalability and invertability (Dinh et al., 2015). We apply generative flow models to reconstruct 3D volumes of a benchmark sandstone sample because its petrophysical properties are fairly well understood. The advantage of this method is that the training is done on 2D images and, afterwards, 3D volume generation is done via a latent space interpolation method. This allows for faster training, reconstruction, and flexibility to incorporate multimodal datatsets from both 2D and 3D imaging methods often used for rock characterization.

*Alternate email address: kmguan@alumni.stanford.edu

To evaluate the quality of synthetic rock images, we consider how well the synthetic volumes mimic the physical properties of the real rock system. Morphological indicators, such as porosity (i.e., void volume fraction) and connectivity, affect the hydrocarbon-producing potential of a reservoir and are directly calculated from the porous media images. Permeability is a measure of fluid flow capacity within the porous system and is related to porosity, the pore shapes, and connectivity as well. The volumes generated are shown to be as useful as the original datasets for computing porosity, permeability, and other rock properties. We verify the accuracy of the generated images by calculating morphological parameters and comparing these against the ground truth rock dataset.

2 METHODS

2.1 GENERATIVE FLOW MODEL

We adapt a preexisting generative flow model to our dataset, specifically one with invertible 1×1 convolutions, coined *Glow*, that has been shown to create realistic-looking, large images (Kingma & Dhariwal, 2018). We start with an implementation of the original *Glow* model (van Amersfoort, 2019) and modify it to load and process our own rock datasets and generate 3D volumes. After the model is trained on the 2D image dataset, we generate a series of anchor slices with a predetermined latent space vector, and interpolate between the anchor slices to create the 3D volume. The interpolation is done by taking a linear combination of the latent space representation of the anchor slices. Further details on the calculation of the latent vectors are described in (Anderson et al., 2020).

2.2 EVALUATION METRICS

2.2.1 MORPHOLOGICAL PARAMETERS

To evaluate the accuracy of our model, we use a set of morphological descriptors known as Minkowski functionals. Minkowski functionals are stereological estimators providing local and global morphological information that is related to single-phase flow mechanisms (Mecke & Arns, 2005; Arns et al., 2010). In 3D, there are four Minkowski functionals that describe the geometric parameters of a set X with a smooth surface ∂X: volume $V(X)$, surface area $S(X)$, integral of mean curvature $\bar{b}(X)$, and Euler-Poincaré characteristic $\chi(X)$, where

$$V(X) = \int_X dx \tag{1}$$

$$S(X) = \int_{\partial X} dx \tag{2}$$

$$\bar{b}(X) = \frac{1}{2\pi} \int_{\partial X} \frac{\kappa_1(x) + \kappa_2(x)}{2}\, dx \tag{3}$$

$$\chi(X) = \frac{1}{4\pi} \int_{\partial X} \kappa_1(x)\kappa_2(x)\, dx \tag{4}$$

and where $\kappa_1(x)$ and $\kappa_2(x)$ with $\kappa(x) = \frac{1}{r(x)}$ are the curvatures corresponding to the maximum and minimum curvature radii, respectively. For discrete images, the functionals are estimated using the *MorphoLibJ* library in ImageJ (Legland et al., 2016; Doube et al., 2010).

We also compute the two-point correlation function, or covariance, of the 3D volume. The two-point correlation function has been used to inform the reconstruction of homogeneous, single-scale media (Jiao et al., 2008). For a binary image, the two-point correlation function represents the probability that two points separated by a lag distance, $\mathbf{r}$, are the same phase. We calculate the directional and radially-averaged correlation function, $S_2(\mathbf{r})$, for the pore phase, P, by

$$S_2(\mathbf{r}) = \mathbf{P}(\mathbf{x} \in P, \mathbf{x} + \mathbf{r} \in P). \tag{5}$$

2.2.2 FLOW PARAMETERS

In addition to porosity, the effective permeability of a porous rock depends on the pore size, geometry, and connectivity. We calculate the single-phase permeability of the generated 3D volumes and

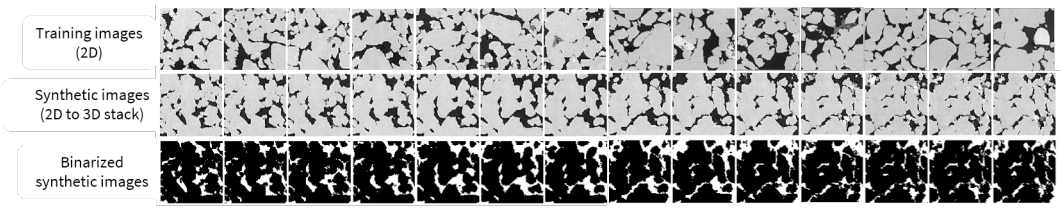

Figure 1: Example of random training image slices and generated image stacks. Image size is 128^2 px. The first and last synthetic images are anchor images and the 12 images in between are interpolated by a linear combination of the latent space representations. The generated images are grayscale initially and then thresholded to yield a binary image stack.

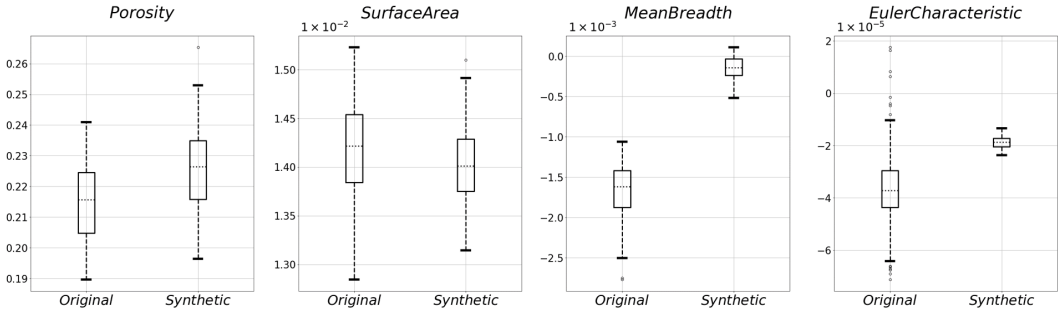

Figure 2: Minkowski functionals - porosity, specific surface area, mean breadth, and Euler-Poincaré characteristic - for the training image set (100 subsampled volumes) and generated images (100 generated volumes).

the real training dataset using identical methods. We use two physics-based methods to compute the single-phase flow: 1) a direct numerical solution (DNS) to the Navier-Stokes equation and 2) a lattice Boltzmann method (LBM) that considers flow to be composed of a collection of pseudo-particles represented by a velocity distribution function (Guan et al., 2019; Crouse et al., 2016). We also obtain the pore-size distribution (PSD) and mercury injection capillary pressure (MICP) directly from the synthetic and training image volumes. The PSD of the imaged rock volume provides information of the entire pore space geometry and MICP is an indicator of drained fluid in a connected pore space environment from one face to the another.

3 Results

3.1 Morphological evaluation

The morphological and petrophysical analyses are performed on the 128^3 voxel volumes of a conventional sandstone rock. Figure 1 shows an example of the training image, generated image stack, and binarized image stack. The first and last images of the synthetic 3D series are anchor images generated from the trained model. The 12 images in between are interpolated using the volume generation method described earlier. We observe in both the grayscale and binarized images that connection of the grain and pore phases is successful throughout the image stack.

The morphological parameters calculated for the training data and synthetic data are shown in Fig. 2. The distribution of porosity, specific surface area, and Euler-Poincaré characteristic between the training and synthetic datasets agree well and have similar margins of error. The second-order functional, represented as the mean breadth, between the two datasets are not in agreement, suggesting differences in the curvature of the generated dataset. We consider single-phase flow in an isotropic sandstone, where the surface-to-volume ratio and topology, represented by the specific surface area and Euler-Poincaré characteristic, respectively, largely affects flow behavior (Mecke & Arns, 2005). For two-phase flow of oil and gas in more complex microporous systems, however, matching the breadth becomes important in order to capture the curved interfaces between the immiscible phases.

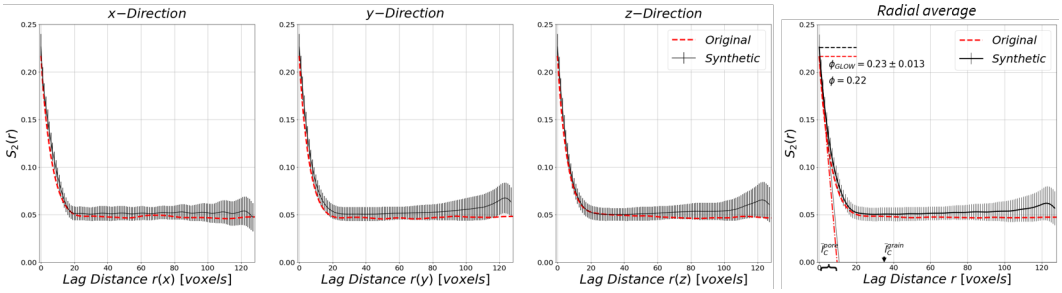

Figure 3: Directional and radially-averaged covariance of the sandstone training image (red) and synthetic volumes (step size = 12).

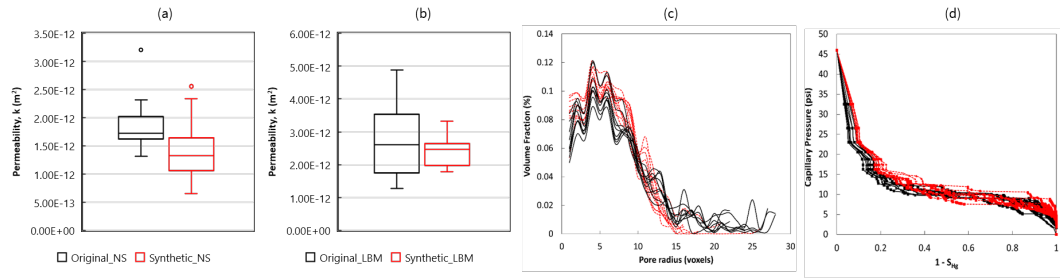

Figure 4: Single-phase permeability for multiple realizations of the sandstone training dataset and generated synthetic images, voxel size of 128^3. Permeability is computed via Navier-Stokes (a) or LBM (b) methods. Pore-size distribution (c) and capillary pressure vs. mercury saturation (d), modeled as drainage along the vertical axis with a constant contact angle for original (black) and synthetic (red) pore volumes.

It is difficult for a single model to match all Minkowski functionals accurately and suggests further refinement or training is needed if studying two-phase flow.

The radially-averaged covariance of the training and synthetic data confirms agreement between the two datasets, as shown in Fig. 3. Both training and synthetic datasets show exponential decay and stabilization at a lag distance of approximately 25 voxels. For the generated samples, the chord length for the pore and solid phases are 11 and 37 voxels, respectively. The similarity between the chord length of the pore phase and the interpolation step size further motivates using the statistical properties of the material to inform the volume generation process.

3.2 Petrophysical comparison

Figure 4 shows the single-phase permeability values obtained from both Navier-Stokes and LBM calculations and the PSD and MICP curves the original training images and generated volumes. The training image volumes were subsampled from the larger micro-CT dataset. We observe a similar distribution of permeability values from the original and synthetic volumes using both computational methods. There is little variability in both training and synthetic volumes. From the MICP graph, we observe that the training dataset has a greater frequency of large pores compared to the synthetic dataset. Given the sensitivity of MICP calculations to small changes in grain shape, as well as the edge effects observed from the covariance curves (Fig. 3), the difference is reasonable. The overall PSD curve and trend of the drainage experiment between the original and synthetic volumes show good agreement. We also note that the pore-size distribution consists primarily of smaller pores below 15 voxels ($91.8\,\mu\text{m}$) with a few large pores in the synthetic and original volumes. The capillary pressure graph confirms the behavior and the percolating pore space (i.e. connected to both the top and the bottom) between the two datasets is similar.

AUTHOR CONTRIBUTIONS

KG performed the NS flow calculations, developed the image evaluation pipeline, and assisted with development of the image synthesis algorithm by testing the algorithm across multiple datasets. TA developed and implemented the presented image volume synthesis algorithm. PC provided the LBM, MICP, and PSD calculations and advised on the project. TK was the principal investigator for this project.

ACKNOWLEDGMENTS

This work was supported as part of the Center for Mechanistic Control of Water-Hydrocarbon-Rock Interactions in Unconventional and Tight Oil Formations (CMC-UF), an Energy Frontier Research Center funded by the U.S. Department of Energy, Office of Science under DOE (BES) Award DE-SC0019165.

We thank Dassault Systèmes for providing computational resources for the LBM calculations. We thank the Stanford Center for Computational Earth & Environmental Sciences (CEES) for providing computational resources for the NS calculations. Part of this work was performed at the Stanford Nano Shared Facilities (SNSF), supported by the NSF under award ECCS-1542152.

REFERENCES

Timothy I. Anderson, Kelly M. Guan, Bolivia Vega, Saman A. Aryana, and Anthony R. Kovscek. Rockflow: Fast generation of synthetic source rock images using generative flow models. *Energies*, 13(24), 2020. ISSN 1996-1073. doi: 10.3390/en13246571. URL https://www.mdpi.com/1996-1073/13/24/6571.

C. H. Arns, M. A. Knackstedt, and K. Mecke. 3D structural analysis: Sensitivity of Minkowski functionals. *Journal of Microscopy*, 240(3):181–196, 2010. ISSN 00222720. doi: 10.1111/j.1365-2818.2010.03395.x.

Bernd Crouse, David M Freed, Nils Koliha, Gana Balasubramanian, Rajani Satti, Derek Bale, and Stephen Zuklic. A Lattice-Boltzmann Based Method Applied to Digital Rock Characterization of Perforation Tunnel Damage. In *International Symposium of the Society of Core Analysts*, pp. 1–6, Snowmass, 2016.

Laurent Dinh, David Krueger, and Yoshua Bengio. NICE: Non-linear independent components estimation. *3rd International Conference on Learning Representations, ICLR 2015 - Workshop Track Proceedings*, 1(2):1–13, 2015.

Michael Doube, Michał M. Kłosowski, Ignacio Arganda-Carreras, Fabrice P. Cordelières, Robert P. Dougherty, Jonathan S. Jackson, Benjamin Schmid, John R. Hutchinson, and Sandra J. Shefelbine. BoneJ: Free and extensible bone image analysis in ImageJ. *Bone*, 47(6):1076–1079, dec 2010. ISSN 8756-3282. doi: 10.1016/J.BONE.2010.08.023. URL https://www.sciencedirect.com/science/article/pii/S8756328210014419.

Junxi Feng, Xiaohai He, Qizhi Teng, Chao Ren, Honggang Chen, and Yang Li. Reconstruction of porous media from extremely limited information using conditional generative adversarial networks. *Physical Review E*, 100(3):33308, 2019. ISSN 24700053. doi: 10.1103/PhysRevE.100.033308. URL https://doi.org/10.1103/PhysRevE.100.033308.

Kelly M. Guan, Marfa Nazarova, Bo Guo, Hamdi Tchelepi, Anthony R. Kovscek, and Patrice Creux. Effects of Image Resolution on Sandstone Porosity and Permeability as Obtained from X-Ray Microscopy. *Transport in Porous Media*, 127(1):233–245, 2019. ISSN 15731634. doi: 10.1007/s11242-018-1189-9. URL https://doi.org/10.1007/s11242-018-1189-9.

Y. Jiao, F. H. Stillinger, and S. Torquato. Modeling heterogeneous materials via two-point correlation functions. II. Algorithmic details and applications. *Physical Review E - Statistical, Nonlinear, and Soft Matter Physics*, 77(3):1–15, 2008. ISSN 15393755. doi: 10.1103/PhysRevE.77.031135.

Richard A. Ketcham and William D. Carlson. Acquisition, optimization and interpretation of x-ray computed tomographic imagery: Applications to the geosciences. *Computers and Geosciences*, 27(4):381–400, 2001. ISSN 00983004. doi: 10.1016/S0098-3004(00)00116-3.

Diederik P. Kingma and Prafulla Dhariwal. Glow: Generative flow with invertible 1×1 convolutions. *Advances in Neural Information Processing Systems*, 2018-Decem:10215–10224, 2018. ISSN 10495258.

David Legland, Ignacio Arganda-Carreras, and Philippe Andrey. MorphoLibJ: integrated library and plugins for mathematical morphology with ImageJ. *Bioinformatics (Oxford, England)*, 32 (22):3532–3534, nov 2016. ISSN 1367-4811 (Electronic). doi: 10.1093/bioinformatics/btw413.

Klaus Mecke and C. H. Arns. Fluids in porous media: A morphometric approach. *Journal of Physics Condensed Matter*, 17(9), 2005. ISSN 09538984. doi: 10.1088/0953-8984/17/9/014.

Lukas Mosser, Olivier Dubrule, and Martin J. Blunt. Reconstruction of three-dimensional porous media using generative adversarial neural networks. *Physical Review E*, 96(4), 2017. ISSN 24700053. doi: 10.1103/PhysRevE.96.043309.

Hiroshi Okabe and Martin J. Blunt. Pore space reconstruction of vuggy carbonates using microtomography and multiple-point statistics. *Water Resources Research*, 43(12):3–7, 2007. ISSN 00431397. doi: 10.1029/2006WR005680.

S Torquato. *Random Heterogeneous Materials: Microstructure and Macroscopic Properties*. Interdisciplinary Applied Mathematics. Springer New York, 2005. ISBN 9780387951676. URL `https://books.google.com/books?id=PhG{_}X4-8DPAC`.

Joost van Amersfoort. Glow-PyTorch. https://github.com/y0ast/Glow-PyTorch, 2019.

J B Walsh and W T Frangos. Permeability of Granite Under High Pressure. *Journal of Geophysical Research*, 73(6), 1968.

Table 1: Normalized flow model architecture and parameters. *Refers to number of epochs to warm up the learning rate from 0 to α

Image size	128^2 pixels
Minibatch size	4
Learning rate, α	5×10^{-4}
Warm up*	5 epochs
Epochs	30
Flow coupling	Additive

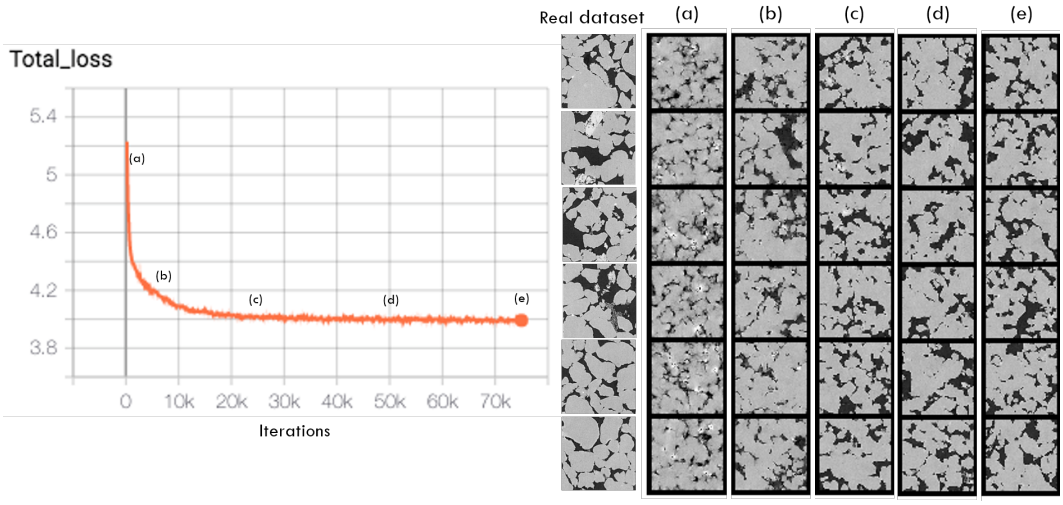

Figure 5: a) Example of training loss for the generative flow model. Training image size $= 128^2$ pixels, batch size $= 4$, learning rate $= 0.0005$, number of epochs $= 30$, flow coupling = additive. b) 128^2 training image set (leftmost column), compared against output of the model during training. The labels a-e correspond to iterations 500, 5000, 25000, 50000, and 75000, as marked in a).

A Appendix

A.1 Training details

We use the default parameters for initial training as detailed in Table 1 below. Figure 5 shows the loss function and output images, respectively, during training the model on 128^2 pixel images. We observe a quick drop in training loss during the first 10k iterations and then little change after 25k iterations. The generated images at different iteration steps show the evolution of the model as it learns to generate the rock images. We observe a noticeable change from 500 to 25k iterations, but afterwards there is little visual difference.

A.2 Interpolation method

Figure 6 shows the relationship between the latent representation of the image image data and the volume generation process. While it would be possible to calculate the number of interpolation steps by minimizing the negative log-likelihood of the generated images across the three Cartesian planes—assuming that the sample volume is isotropic and homogeneous—this method is time-intensive when evaluating over a large range of possible interpolation steps. Instead, we use the average pore chord length, calculated from the two-point correlation function across the $x - y$ directions, to inform the appropriate step size in the z direction. This method allows for a hybrid approach of using statistical properties to inform the final 3D reconstruction of images that were trained via a deep-learning method.

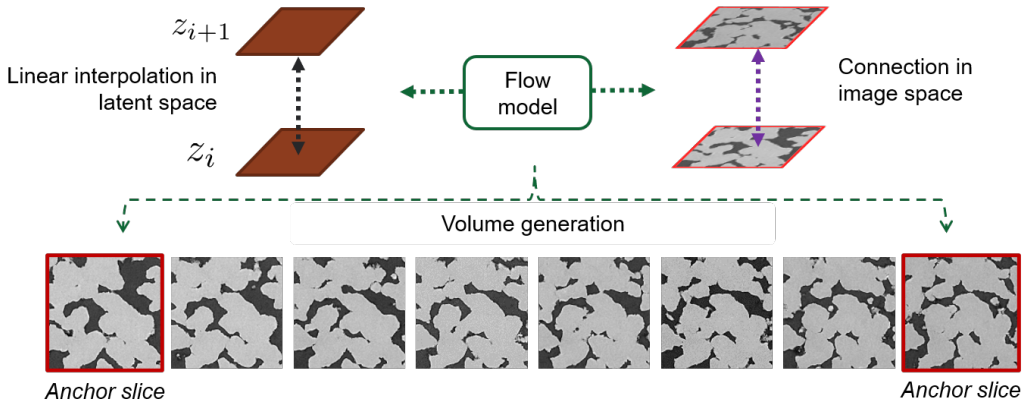

Figure 6: Diagram showing how a linear interpolation of vectors in the latent space leads to a connected volume between two synthetically-generated anchor slices in the image space. Figure adapted from Anderson et al. (2020)

.

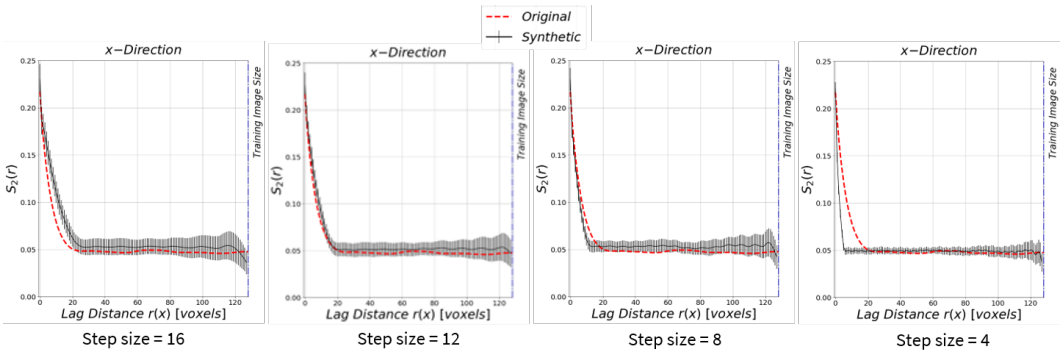

Figure 7: Directional covariance of the sandstone compared against the synthetic volume in the interpolating (x) direction for different interpolation step sizes. A step size of 12 shows the best agreement with the directional covariance of the original training dataset (red).

We determine the average chord length for the pore and solid phases from the slope of two-point correlation function at the origin (Torquato, 2005),

$$\bar{l}_c^{pore} = \frac{\phi}{S_2'(0)} \tag{6}$$

$$\bar{l}_c^{solid} = \frac{1-\phi}{S_2'(0)}. \tag{7}$$

The chord is the length between intersections of a line with the pore solid interface. The chord length is especially interesting to address heterogeneous pore structures because it provides a measure of structural disorder.

Figure 7 shows the effect of modifying the interpolation step size on the directional covariance in the interpolation plane (x). We observe the best match between the training and synthetic dataset at a step size of 12 interpolated images. At a step size of 16, the covariance at short lag distances diverges. At step sizes of 8 and 4, the covariance exhibits periodic patterns that are not in the training dataset and do not match the original dataset at short lag distances either. For the remaining results, we use a step size of 12. The directional and radially-averaged covariance for this step size is shown in Fig. 3 and indicates that the generated images capture the two-point statistics in all directions reasonably well. We observe some edge effects after 110 voxels that been observed with GAN-

generated images as well and can be resolved by cropping the image accordingly (Mosser et al., 2017).

The average chord length of the pore space, a statistical property, is useful to inform accurate 3D generation of a model trained on a 2D dataset. The agreement of the two-point correlation function and Minkowski functionals support this method. As shown in Fig. 7, step size has an important effect on the 3D statistical properties of the generated volume. The step size during interpolation refers to the number of intermediate images generated in between a pair of anchor slices. Deviations between the original and synthetic sample primarily occurred at small lag distances and demonstrate the difficulty of capturing the short-range properties in all directions. Deviations at larger lag distances may indicate overfitting or that long-range properties were not completely captured during training. Small step sizes appear to match the long-range properties better, but exhibit periodic behavior that is not seen in the original sample.